Structures of DNA-Linked Nanoparticle Aggregates

Sung Yong Park, Jae-Seung Lee, Dimitra Georganopoulou, Chad A. Mirkin, and George C. Schatz*

Department of Chemistry, Northwestern University, Evanston, Illinois 60208

Received: April 10, 2006

The room-temperature structure of DNA-linked gold nanoparticle aggregates is investigated using a combination of experiment and theory. The experiments involve extinction spectroscopy measurements and dynamic light scattering measurements of aggregates made using 60 and 80 nm gold particles and 30 base-pair DNA. The theoretical studies use calculated spectra for models of the aggregate structures to determine which structure matches the observations. These models include diffusion-limited cluster-cluster aggregation (DLCA), reaction-limited cluster-cluster aggregation (RLCA), and compact (nonfractal) cluster aggregation. The diameter of the nanoparticles used in the experiments is larger than has been considered previously, and this provides greater sensitivity of spectra to aggregate structure. We show that the best match between experiment and theory occurs for the RLCA fractal structures. This indicates that DNA hybridization takes place under irreversible conditions in the room-temperature aggregation. Some possible structural variations which might influence the result are considered, including the edge-to-edge distance between nanoparticles, variation in the diameter of the nanoparticles, underlying lattice structures of on-lattice compact clusters, and positional disorders in the lattice structures. We find that these variations do not change the conclusion that the room-temperature structure of the aggregates is fractal. We also examine the variation in extinction at 260 nm as temperature is increased, showing that the decrease in extinction at temperatures below the melting temperature is related to a morphological change from fractal toward compact structures.

1. Introduction

DNA-linked nanocomposite systems have attracted significant interest recently as a result of important advances in nanotechnological applications related to self-assembly and molecular recognition.[1−11] Among these systems, DNA-linked gold nanoparticle aggregates have attracted particular attention, as the chemical or physical property changes during DNA-mediated aggregation can be used for biosensing. Aggregate formation in this case occurs when gold particles functionalized with single-stranded oligonucleotides are mixed with a target of complementary DNA. Hybridization leads to the formation of a polymeric network in which the distance between the gold particles is determined by the length of the duplex. Electromagnetic couplings between the nanoparticles lead to a red-shift of the plasmon resonance upon aggregation, which in the case of 13 nm gold particles that are separated by 30 base-pair DNA corresponds to a spectral shift from 520 nm (for the isolated particle) to 574 nm.[12] The size of this shift depends on particle size, length of DNA, and the structure of the aggregate.[5,12−14]

Under ordinary conditions, DNA hybridization in solution is a reversible process. For aggregates formed from 13 nm gold particles, it is possible to prepare aggregates under reversible conditions by cooling slowly from high temperatures. This leads to the formation of compact clusters.[14−16] However, at low temperatures such as room temperature, the situation may be different, as pointed out in refs 12 and 17. In this case, kinetic structures result because the rate of dissociation of DNA can be slower than the time scale of aggregation, while the association rate is faster. This leads to the possibility of fractal aggregate formation at low temperatures, which is well-known in other applications involving colloidal aggregation.[18]

In this paper, we present experiments and theory which provide new insight concerning DNA-linked gold particle aggregates through the study of aggregates built from 60 or 80 nm gold particles. These larger particles have many advantages in studies of the aggregate structure. First, the number of nanoparticles in the aggregates is much smaller. This makes it possible to do higher-quality computational studies of the spectra of the aggregates in which the particles are explicitly described with converged electrodynamics. Second, the extinction spectra are more sensitive to details of the aggregate structure than for smaller particles, due to the stronger electrodynamic couplings between the particles. This makes it possible to distinguish between different structural models, and from this to determine the conditions that produce fractal structures or compact structures.

A striking property of the aggregates is that they exhibit melting transitions well above room temperature that are considerably narrower than are found for the same DNA duplexes in solution.[1,12,19−21] This result, which has been the subject of significant theoretical and experimental interest,[3,4,14,15,17,19,22−26] is not considered in this paper. However, we do consider a related observation, which is that, below the sharp melting transition, unannealed aggregates show monotonic decrease of extinction with increasing temperature. Similar behavior has been reported in various other unannealed DNA-linked nanocomposite aggregates which show sharp melting.[3,9,10] Here, we examine the temperature dependence of the extinction spectra below the melting temperature to study the importance of aggregate restructuring that occurs as the melting temperature is approached.

* Email: schatz@chem.northwestern.edu.

2. Structural Models of Aggregation

In this section, we describe models that we have considered for the formation of DNA-linked gold nanoparticle aggregates at low (room) temperature. This part of our analysis follows closely the earlier discussion in ref 17. A key factor in this discussion is whether the aggregation process is reversible or not, and the guiding principles in answering this question are the kinetics and thermodynamics of DNA hybridization. An often-used model of the hybridization of short oligonucleotides is the "two-state" model, in which the DNA is assumed to be in one of two states, hybridized or dehybridized, that are in equilibrium. The rate of transition between hybridized and dehybridized states has sometimes been measured for DNA in solution, and it is found that, while the association step has a relatively small activation energy, the activation energy for dissociation is very high (9.94 kcal/mol (association) and 53.4 kcal/mol (dissociation) for a 10-mer, and 16.4 kcal/mol (association) and 112 kcal/mol (dissociation) for a 20-mer as measured in ref 27). While the kinetics of hybridization in DNA-linked gold nanoparticle aggregates has not been studied in detail, it seems likely that similar rates will apply individually to each DNA, although the overall aggregate formation rate is also limited by diffusion of the nanoparticles. However, a key point is that at room temperature the dissociation rate of DNA duplexes is so small that the aggregation process occurs more rapidly than the restructuring of kinetic structure that arises from DNA dehybridization, and aggregate formation is therefore irreversible.

Under these circumstances, two limiting regimes of irreversible kinetic colloid aggregation can be identified, both of which lead to the formation of fractal aggregates: rapid, diffusion-limited cluster-cluster aggregation (DLCA) and slow, reaction-limited cluster-cluster aggregation (RLCA). In DLCA, it is assumed that the nanoparticles stick whenever they collide, whereas in RLCA, it is assumed that there is a barrier to sticking such that numerous collisions are needed to produce sticking. In the past work,[17] it was assumed that, because there is a barrier to DNA association, aggregation should be of the RLCA type, for which the fractal dimension is 2.07. Here, we also consider the possibility of DLCA, which leads to the formation of less dense aggregates with a fractal dimension of 1.78. Note that, as temperature increases, the above argument, based on irreversible binding, is no longer valid, since DNA dehybridization may easily take place, and the aggregate can restructure into compact and nonfractal structures.[18]

One feature of the fractal aggregation process which we discuss here is that the aggregates have a highly polydisperse distribution. In RLCA, it is well-known that the cluster mass distribution, i.e., the distribution of the number of particles inside each cluster, has a power-law form with an exponential cutoff, where the cutoff mass grows exponentially as a function of the time elapsed.[28] Thus, the cluster size distribution provides a signature of fractal aggregation which contrasts with that for equilibrium aggregation processes.[29]

In this paper, we numerically generate RLCA, DLCA, and compact clusters and calculate the extinction cross section to compare with UV–vis measurements to compare with the experiments. For the RLCA clusters, we used the lattice-based reaction-limited cluster-cluster aggregation model of refs 18 and 30 to generate structures. In this algorithm, we consider the distribution of clusters on a cubic lattice. Initially, this distribution will consist of N individual nanoparticles. Two clusters (initially two particles) are chosen and positioned at random in a large box. If this results in the clusters being adjacent but not

overlapping, the new configuration is accepted as a single merged cluster. We continue this procedure until the distribution becomes a single large cluster. This implicitly assumes that the reaction time to make a bond between two adjacent clusters is much larger than the diffusion time of the clusters and that the solution is very dilute, so that we assume that every pair of clusters has an equal chance to meet with any possible position.

To generate DLCA clusters using a lattice-based model, we follow the method described in refs 31 and 32. In this simulation, we consider a simple cubic lattice with periodic boundary conditions. At the start of the simulation, N individual nanoparticles are randomly distributed throughout the lattice. Particles are allowed to diffuse one lattice site at a time, and they merge into clusters whenever they become located on adjacent sites. The merged clusters are assumed to be rigid, and they diffuse like individual particles. Once all N particles have merged into a single cluster, we stop the simulation.

Finally, compact clusters can be obtained from a reversible model that is described in ref 17. In this model, which is based on the idea that the equilibrium state at a given temperature is independent of the path which the system follows to get there, we consider the dissociation process due to DNA dehybridization and the association process due to DNA hybridization separately. Thus, for the association, we apply the reaction-limited cluster-cluster aggregation model described above. For the dissociation, we apply a bond-percolation model. In this model, we consider a large cluster on a simple cubic lattice that is generated by the association process. Initially, all two-particle pairs on nearest-neighbor sites are considered as linked so that nanoparticles in the large cluster are all connected. In each step of the simulation, we assume that the link between an adjacent pair of particles is broken with a probability $1 - p$. After applying this probability to all particle pairs, we check the connectivity of each particle and use this to split the large cluster into a set of connected smaller clusters. This set is used as an initial distribution for an RLCA association process. It turns out that the probability p is related to the proportion of total single strands to double strands in the cluster at a given temperature,[17,22] and thus, this algorithm generates the correct aggregate morphology for a given temperature. In the present application, we have only considered $p = 0.95$, as this generates a relatively compact cluster associated with a temperature that is much lower than the melting temperature.

3. Calculation of Optical Properties

Given the cluster morphologies that we have generated, we now calculate their extinction cross sections using two methods: the discrete dipole approximation (DDA)[33−35] and a T-matrix coupled multipole method.[36−39] We assume that light scatters from an isolated aggregate in aqueous solution, and thus, we ignore the contribution of the multiple scattering between aggregates.

3.1. Discrete Dipole Approximation. In the DDA method, the object is taken to be an array of induced point dipoles ($i = 1, ..., N_d$) with dipole moments $\mathbf{P}_i$ and polarizabilities α_i located at positions $\mathbf{r}_i$. For this application, we consider one dipole for each particle in the cluster, and thus, $N_d = N$, where N is the number of nanoparticles. We consider that particles in the cluster are spheres with radius a, so that we can obtain the polarizabilities α_i from the finite-size-corrected dielectric function which can be calculated using tabulated bulk values as in refs 14, 15, and 17. If $\mathbf{E}_i$ denotes the electric field at $\mathbf{r}_i$, the position

Structures of DNA-Linked Nanoparticle Aggregates

J. Phys. Chem. B, Vol. 110, No. 25, 2006 **12675**

of a particle in the cluster, we can write the polarization $\mathbf{P}_i$ as

$$\mathbf{P}_i = \alpha_t \mathbf{E}_i \qquad (1)$$

where the electric field at $\mathbf{r}_i$ is the sum of the electric field of the incident light $\mathbf{E}_{\text{inc},i} = \mathbf{E}_0 \exp(i\mathbf{k}\cdot\mathbf{r}_i - i\omega t)$ plus the scattered field from the other particles

$$\mathbf{E}_i = \mathbf{E}_{\text{inc},i} - \sum_{j\neq i}\mathbf{A}_{ij}\cdot\mathbf{P}_j \qquad (2)$$

The product $\mathbf{A}_{ij}\cdot\mathbf{P}_j$ can be expressed as

$$\mathbf{A}_{ij}\cdot\mathbf{P}_j = \frac{\exp(ikr_{ij} - i\omega t)}{r_{ij}^3}\left\{ k^2\mathbf{r}_{ij}\times(\mathbf{r}_{ij}\times\mathbf{P}_j) + \frac{1 - ikr_{ij}}{r_{ij}^2}[r_{ij}^2\mathbf{P}_j - 3\mathbf{r}_{ij}(\mathbf{r}_{ij}\cdot\mathbf{P}_j)] \right\} \qquad (3)$$

Here, $\mathbf{r}_{ij} = \mathbf{r}_i - \mathbf{r}_j$ and $k = \omega/c \equiv 2\pi/\lambda$, c and λ being the speed of light and wavelength in a vacuum. Equations 1–3 form a couple sets of $3N$ equations, which can be solved for the N dipole moments $\mathbf{P}_i$ using the complex-conjugate gradient method combined with fast Fourier transforms.[34] Given the $\mathbf{P}_i$'s, the extinction cross section C_{ext} for a given cluster is obtained from the relation

$$C_{\text{ext}} = \frac{4\pi k}{|\mathbf{E}_0|^2}\,\text{Im}[\sum_{j=1}^{N}\mathbf{E}_0^*\exp(-i\mathbf{k}\cdot\mathbf{r}_j)\cdot\mathbf{p}_j] \qquad (4)$$

where the sum runs over the N particles in the cluster.

3.2. *T*-Matrix Method. The *T*-matrix coupled multipole method provides an efficient method for modeling the electrodynamics of spherical particles with arbitrary radius and positions. For a cluster of metal spheres that have a diameter D of ∼60 nm or more, the dipole representation of the field for each sphere often is not adequate to predict the cluster optical properties. Instead, one needs to consider higher multipole orders, and in the approach we use, the order is determined dynamically so as to generate converged results. The theory to do this was first developed in the early 1970s,[36,37] and it has been widely used since the mid-1990s.[38,39]

We consider a cluster in which nanoparticles are spheres and the number of the nanoparticles is N. The scattered electric field of the cluster is taken as a superposition of fields from each sphere in it, i.e.

$$E_s = \sum_{i=1}^{N}E_s^i \qquad (5)$$

E_s^i, the scattered field of an individual sphere, is expanded in vector spherical harmonics and expressed as

$$E_s^i = \sum_{n=1}^{\infty}\sum_{m=-n}^{n}\sum_{p=1}^{2}a_{mnp}^i h_{mnp}(kr^i, \theta^i, \phi^i) \qquad (6)$$

where n and m specify the order and degree of the spherical harmonics $h_{mnp}(kr^i, \theta^i, \phi^i)$, a_{mnp}^i are expansion coefficients, $k = 2\pi/\lambda$ is the wavenumber of the incident radiation having wavelength λ, and r^i, θ^i, and ϕ^i are the spherical coordinates of sphere i. The index p denotes the modes of the scattered field, with $p = 1$ referring to transverse magnetic modes (TM) and $p = 2$ to transverse electric modes (TE) for which there is no radial magnetic and electric field component, respectively.

By applying electromagnetic field boundary conditions at each sphere and employing addition theorems in which harmonics about one origin are expanded as harmonics about another origin, one obtains a system of equations for the scattered-field expansion coefficients for all the spheres in the cluster. After truncating the expansions in eq 6 to $n = N_t^i$, one obtains a system of equations

$$a_{mnp}^i + \bar{a}_{np}^i\sum_{\substack{j=1 \\ j\neq i}}^{N}\sum_{l=1}^{N_t^j}\sum_{k=-l}^{l}\sum_{q=1}^{2}H_{mnpklq}^{ij}a_{klq}^j = \bar{a}_{np}^i p_{mnp}^i \qquad (7)$$

where q denotes the TM and TE modes. H_{mnpklq}^{ij} denotes the Hankel-function-based addition coefficients, $\bar{a}_{np}^i$ are the TM and TE Lorenz/Mie coefficients, and p_{mnp}^i are the expansion coefficients for the incident wave at the origin of sphere i. After formally inverting eq 7, one finds a transition matrix T for the cluster of spheres as

$$a_{mnp}^i = \sum_{j=1}^{N}\sum_{l=1}^{N_t^j}\sum_{k=-l}^{l}\sum_{q=1}^{2}T_{mnpklq}^{ij}p_{klq}^j \qquad (8)$$

Here, the *T*-matrix refers to the individual scattered fields from each sphere in the cluster. To describe the scattered field from the cluster as a whole, it is necessary to combine the superimposed fields from the cluster into a single field based on a single coordinate origin. The expansion coefficients representing the total scattered field are then given by

$$a_{mnp}^0 = \sum_{i=1}^{N}\sum_{l=1}^{N_t^i}\sum_{k=-l}^{l}\sum_{q=1}^{2}J_{mnpklq}^{0i}a_{klq}^i \qquad (9)$$

where J_{mnpklq}^{0i} are addition coefficients based on Bessel functions. In a similar way, the expansion coefficients for the incident field at the origin of sphere i, p_{mnp}^i, can be obtained by

$$p_{mnp}^i = \sum_{l=1}^{N_t^0}\sum_{k=-l}^{l}\sum_{q=1}^{2}J_{mnpklq}^{i0}p_{klq}^0 \qquad (10)$$

after truncating the expansion of the total scattered field at $n = N^0$. Inserting eq 8 and eq 10 into eq 9, one obtains

$$a_{mnp}^0 = \sum_{l=1}^{N^0}\sum_{k=-l}^{l}\sum_{q=1}^{2}T_{mnpklq}^0 p_{klq}^0 \qquad (11)$$

where

$$T_{mnpklq}^0 \equiv$$
$$\sum_{i=1}^{N}\sum_{n'=1}^{N_t^i}\sum_{m'=-n'}^{n'}\sum_{p'=1}^{2}\sum_{j=1}^{N}\sum_{l'=1}^{N_t^j}\sum_{k'=-l'}^{l'}\sum_{q'=1}^{2}J_{mnpm'n'p'}^{0i}T_{m'n'p'k'l'q'}^{ij}J_{k'l'q'klq}^{j0} \qquad (12)$$

With this information, the orientation-averaged extinction cross section C_{ext} is expressed as

$$C_{\text{ext}} = \frac{2\pi}{k^2}\,\text{Re}(\sum_{n=1}^{N^0}\sum_{m=-n}^{n}\sum_{p=1}^{2}T_{mnpmnp}^0) \qquad (13)$$

4. Experimental Section

The gold nanoparticles (Au NPs, 60 and 80 nm) were purchased from Ted Pella, Inc. 5′- and 3′-thiol-modified DNA

strands were purchased from Integrated DNA Technologies with HPLC purification. All the buffers and aqueous solutions were prepared with nuclease-free water (Ambion). All the chemicals were purchased from Sigma-Aldrich except dithiothreitol (DTT, Pierce) and used as received.

DNA functionalization of Au NPs was prepared through chemisorption of the terminal monothiol group of DNA strands onto the Au NP surface following our previous literature procedure.[19] Typically, terminal disulfide groups of the DNA strands were cleaved and reduced to monothiols by soaking in 0.1 M DTT in 0.17 M phosphate buffer (PB) solution (pH = 8.0) for 2 h and purified with a NAP-5 column (GE Health Care) to remove excess DTT. 1 OD of the thiol-modified DNA was added to 1 mL of Au colloid solutions and incubated overnight at room temperature under gentle shaking.

The salt concentration was brought to 0.3 M NaCl in the PBS (Phosphate Buffer Saline, 0.01% SDS, pH = 7.4, 10 mM phosphate) by an initial addition of 0.1 M PB and 1% SDS in 0.1 M PB followed by five equal additions of 2 M NaCl over a 2-day period. The final solution was incubated overnight at room temperature. The colloid was washed three times with 0.3 M NaCl PBS (0.005% Tween 20, pH = 7.4, 10 mM phosphate) by centrifugation and removal of supernatant in order to remove excess DNA strands in the solution. The washed particles were finally redispersed in 0.3 M NaCl PBS and stored at 4 °C until use. For high reproducibility, the same batches of Au NPs and buffers were used for all the experiments.

The molar concentrations of the Au NPs were determined by a UV−vis spectrometer (Cary 5000) using Beer's law (molar extinction coefficients are 2.9×10^{10} M^{-1} cm^{-1} at λ_{539} for 60 nm particle and 6.9×10^{10} M^{-1} cm^{-1} at λ_{550} for 80 nm particle).[40] 13.4 fmol of each 60 nm particle (5′- and 3′-) and 5.6 fmol of each 80 nm particle (5′- and 3′-) were mixed, respectively. Linker DNA strands at 100 times excess in 0.3 M NaCl PBS was added to each set of particles to give a final volume of 1.5 mL in a 1.5 mL eppendorf tube. The final NP concentrations were 8.93 pM for 60 nm particles and 3.73 pM for 80 nm particles. The eppendorf tubes were rotated on a rotisserie rotator at 8 rpm to minimize the gravitational effect on the formation of the aggregates during the hybridization process. Importantly, the tubes were fully filled with the reaction solution so that there was no empty space in the solution while being rotated.

The UV−vis spectra of the hybridized DNA−Au NPs were obtained at 1 h and at 5 h after mixing and compared with those of unhybridized Au NPs. The solutions were agitated before the optical spectra were measured to ensure the homogeneity of the particle suspension. To remove a discontinuity at 800 nm which was caused by the change of the lamps and the detectors of the spectrometer, the spectrum region from 800 to 850 nm was omitted for clarity. The melting curves of 60 and 80 nm DNA−Au NPs were obtained by monitoring changes in extinction at 260 nm. The temperature was increased from 25 °C to 80 °C at a rate of 1 °C/min. To maintain a homogeneous system, the solution was stirred continuously with a magnetic stir bar.

Dynamic light scattering measurements were carried out using a Zetasizer Nano ZS (Malvern Instruments). Incident light was provided by a He−Ne laser (λ_{ex} = 633 nm) operating at 4 mW. Scattered light was collected at a fixed angle of 173°. The DNA−Au NP aggregate samples were prepared as described above. Ten runs were performed, each with a run duration of 10 s.
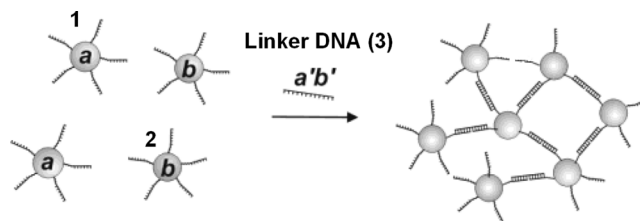
1. 5′ SH(CH$_2$)$_6$-A$_{10}$-CGTCGCATTCAGGAT 3′
2. 3′ SH(CH$_2$)$_3$-A$_{10}$-TCGATGGTCAACTCT 5′
3. 3′ GCAGCGTAAGTCCTA-AGAGTTGACCATCGA 5′

Figure 1. Schematic representation of DNA-linked nanoparticle aggregation. We also present the full sequences for the two probes, **1** and **2**, which bind to the linker DNA **3**.
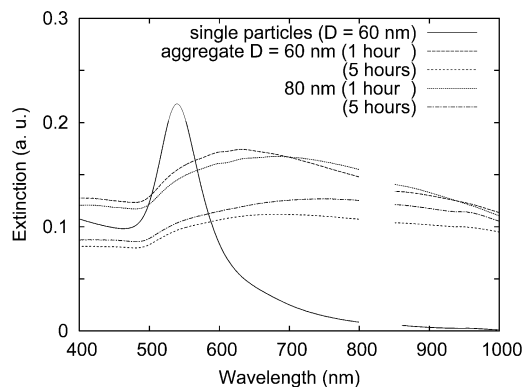

Figure 2. UV−vis spectra of DNA-linked nanoparticles (the diameter D = 60 and 80 nm) with linker DNA strands at room temperature 1 h or 5 h after the hybridization. For comparison purposes, we also include the UV−vis spectra of DNA-linked nanoparticles (D = 60 nm) without linker strands (solid line), but scaled to a similar intensity as that of the aggregates.

5. Results

5.1. Experimental Results. Our approach to investigate the effect of size of the Au nanoparticles on the optical properties of their hybridized aggregate is illustrated in Figure 1. Two batches of Au particles (**a** and **b**) are functionalized with 5′- and 3′-thiol DNA strands (**1** and **2**, respectively) that had polyadenine (10-mer) spacers and 15 base recognition sequences. They were designed to recognize the complementary 30-mer linker sequence (**3**) and to be assembled into aggregate structures. The hybridization process was apparent both visually and by the UV−vis spectrometer at 260 or 535 nm.

We measured UV−vis spectra of the DNA-linked Au nanoparticle aggregates, and the results are shown in Figure 2, along with results for the 80 nm particles before aggregation. Here, we have rotated the tube at 8 rpm during the experiment, and the spectra were taken after 5 h of hybridization. Two types of unhybridized Au nanoparticles (60 and 80 nm) were characterized showing the plasmon bands centered at 539 nm for 60 nm particles and 550 nm for 80 nm particles, respectively. The dark red Au solutions became purple after addition of the linker DNA strands. Without rotation of the tube, we can usually observe formation of black macroscopic precipitated aggregates after the hybridization has proceeded for a couple of hours, but with the rotation of tube (8 rpm), we cannot observe formation of macroscopic aggregates even 5 h after the hybridization. After 5 h, broad maxima were obtained in the spectra at around 670 nm for the hybridized 60 nm particle aggregate, and at around 750 nm for the hybridized 80 nm particle aggregate. These peaks arose from the aggregates. Importantly, both of these aggregate peaks are red-shifted from the value that is obtained with 13 nm gold particles.[12]

Structures of DNA-Linked Nanoparticle Aggregates

*J. Phys. Chem. B, Vol. 110, No. 25, 2006* **12677**
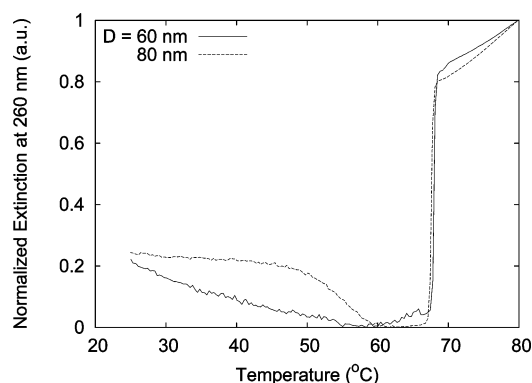
Figure 3. Temperature dependence of the extinction at 260 nm of DNA-linked Au nanoparticle aggregates. The diameters D of nanoparticles are 60 and 80 nm. The extinction at 260 nm was recorded at 1 °C intervals at a rate of 1 min/deg from 25 to 80 °C.

Dynamic light scattering was performed on the DNA-linked gold nanoparticle aggregates to estimate their size. In this experiment, we used the same sample used in monitoring aggregation by UV−vis spectroscopy (vide supra). In the case of 60 nm aggregates, after 1 h, the hydrodynamic radius a_H is found to have a distribution from 150 to 300 nm with a maximum at 210 nm, and after 5 h, it has a distribution from 230 to 410 nm with a maximum at 310 nm. These ranges do not include contributions from a long time tail in the intensity autocorrelation function that was also observed (described in the Supporting Information). However, even without this, the results indicate that the aggregates formed at low temperature are polydisperse. Unfortunately, the cluster size distribution is too poorly defined to enable a meaningful comparison with the predictions noted earlier concerning fractal aggregates; however, later we will use the radius results to estimate cluster sizes in our analysis of Figure 2.

We have also investigated the temperature dependence of the extinction for the 60 and 80 nm aggregates, starting with aggregates that were prepared at room temperature. Here, we have monitored the extinction at 260 nm, while increasing the temperature of the solution at a rate of 1 °C per minute. As presented in Figure 3, there is a sharp increase in the extinction at 68 °C, which is related to the sharp melting transition associated with DNA dehybridization that has been described previously.[3,12,19] Below the melting temperature, we observe that the extinction at 260 nm gradually decreases as we increase the temperature. This tendency is similar to that observed in DNA-linked nanoparticle systems with smaller particle diameters,[3] and it is also found in DNA-linked aggregates that do not contain gold particles.[9,10]

5.2. Numerical Results. We turn now to our numerical results, beginning with the structural properties of the aggregates based on the DLCA, RLCA, and compact models. First, we show that our numerical algorithm does indeed generate clusters with the correct fractal dimensions. In Figure 4, we show some typical cluster morphologies for each aggregation model based on calculations with $N = 400$ nanoparticles. The fractal aggregates have the form of randomly connected polydisperse small clusters, since irreversible binding prohibits restructuring. To check whether we generate the correct structures, we have calculated the fractal dimension d_f from the size dependence of the radius of gyration R_g of the clusters. Here, the radius of gyration R_g is defined by the relation
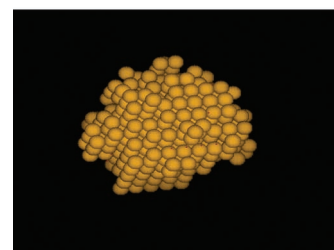
$$R_g^2 = \frac{1}{N}\sum_{i=1}^{N}|\mathbf{r}_i - \bar{\mathbf{r}}|^2 \qquad (14)$$
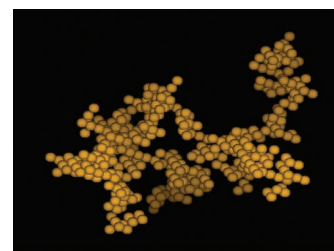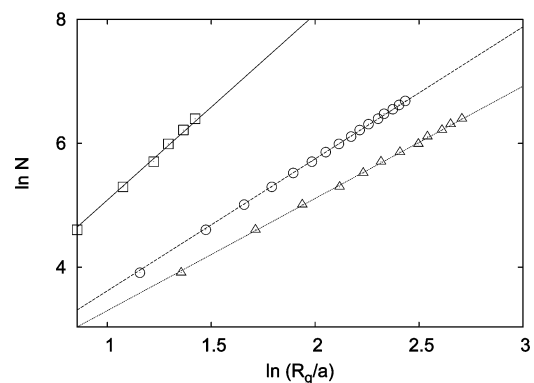

(a)
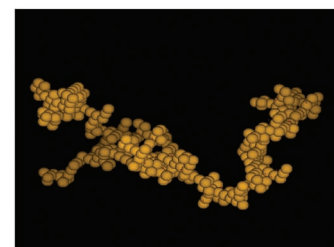
(b)

(c)

Figure 4. Typical morphology of a cluster with the number of nanoparticles $N = 400$: (a) a reaction-limited cluster-cluster aggregate; (b) a diffusion-limited cluster-cluster aggregate; (c) a compact cluster.


Figure 5. Log−log plot of the number of nanoparticles N for RLCA (open circle), DLCA (open square), and compact (open triangle) clusters, plotted as a function of the radius of gyration R_g. Here, a denotes the radius of nanoparticles. Lines show least-squares fits. The slopes of the lines, which represent the fractal dimensions of each cluster, are 3.0 (solid line), 2.1 (dashed line), and 1.8 (dotted line), consistent with expectations for compact, RLCA, and DLCA clusters, respectively.

where $\mathbf{r}_i$ is the position of the ith nanoparticle and $\bar{\mathbf{r}} = N^{-1}\sum_i \mathbf{r}_i$ is the cluster center of mass. Then, the fractal dimension d_f is given by

$$d_f = \lim_{R_g \to \infty} \frac{d \ln N}{d \ln R_g} \qquad (15)$$

Figure 5 shows log−log plots of N against R_g for all three models, where for each model we averaged over 100−1000
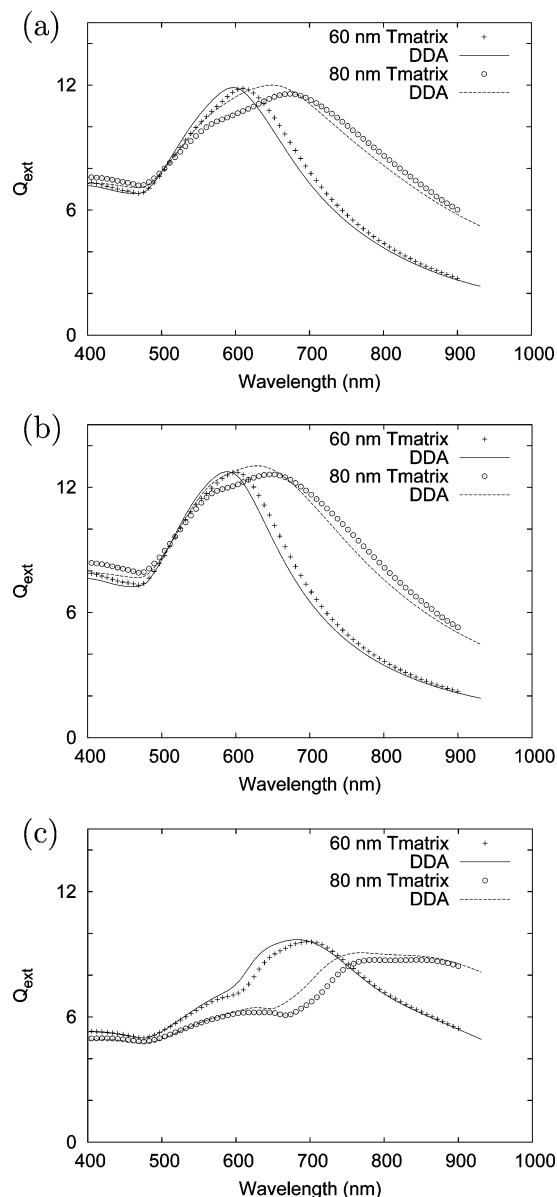
Figure 6. Extinction coefficients Q_{ext} for nanoparticle aggregates in an aqueous solution, calculated using two different methods. Solid lines and dashed lines indicate DDA results, and crosses and open circles indicate *T*-matrix results for (a) a RLCA cluster; (b) a DLCA cluster; (c) a compact cluster. The number of nanoparticles *N* is 100. The results were averaged over 10 different realizations of each cluster.

different realizations of each cluster for each *N*. The log−log plots are accurately fit using straight lines with slopes $d_f = 1.8$, 2.1, and 3.0, for the DLCA, RLCA, and compact cluster models, respectively. Thus, we confirm that each algorithm generates the right morphologies for the structures we are considering.

Next, we turn to the calculated optical properties of the clusters. Here, we assume that the nanoparticles in an aqueous solution have spherical shapes and are made of gold. The contribution of DNA to the optical properties is not considered, since for wavelengths above 400 nm, the contribution of DNA to the extinction is not significant.[14,15]

First, we compare DDA results with the (exact) *T*-matrix method. In Figure 6, we present the extinction coefficients calculated from the two methods for each cluster model and for each particle diameter. The number of particles in each cluster is 100, and we averaged over 10 different realizations of each cluster for each data point plotted using an algorithm from ref 30. For the dielectric function of the gold nanoparticles,

we used a finite-particle-size corrected dielectric function, as estimated from the tabulated values for bulk gold.[14,15,17]

For the results in Figure 6, the closest distance between the nanoparticle surfaces, which we call the edge-to-edge distance in what follows, is taken to be 12 nm, based on the measured results from small-angle X-ray scattering (SAXS) experiments.[16] The measured results refer to 12 nm gold particles linked by 24 base-pair DNA, and different salt concentrations than are considered here so let us briefly discuss why we assume a 12 nm edge-to-edge separation. Since the length per base pair of B-form DNA is 0.34 nm[41] and the length of the surface-binding alkanethiol is 0.7 nm, the fully stretched edge-to-edge distance between a nanoparticle pair connected by 30 base-pair hybridized DNA and 10 base spacers on each end of the DNA would be 18.4 nm. In the SAXS experiment,[16] the edge-to-edge distance was measured to be 7.7 nm in the case of 24 base linkers and $D = 12$ nm gold nanoparticles linked with 12 base DNA sequences and no spacer at 0.3 M PBS solution. If a 10 base adenine spacer is added to each 12 base sequence, the distance is extended by 1.6 nm. Also, for 0.1 M solution which was the salt concentration used in our experiment, the edge-to-edge distance is increased to 8.4 nm. To estimate the edge-to-edge separation for 30 base linkers, 15 base recognition sequences, and 10 base adenine spacers, we scale the 8.4 nm result by 30/24 and add 1.6 nm. This assumes that the edge-to-edge distance does not depend on the size of the particle, which unfortunately cannot be separately verified; however, later we will test the sensitivity of the results to edge-to-edge spacing.

Figure 6 shows that the DDA and *T*-matrix results are generally consistent, but with the position of the plasmon peak being 6−14 nm higher in the *T*-matrix results than in DDA for both particle diameters. Since it is not feasible to do *T*-matrix calculations for clusters with more than 100 particles, we will use DDA calculations in our studies below. However, we should keep in mind that the final results need to be adjusted to longer wavelengths by a few nanometers to describe the effect of multipolar interactions which are included in *T*-matrix theory but not in DDA.

Next, we examine with the DDA method the dependence of the extinction spectra on the number of particles in the cluster. Figure 7 shows results for the three different aggregate structure models (DLCA, RLCA, and compact) for $D = 60$ nm particles, while Figure 8 shows the corresponding results for the $D = 80$ nm particles. The results for the DLCA clusters (see Figure 7b) show that the peak position does not depend significantly on the number of particles in the cluster, with the peak positions being about 600 nm for $D = 60$ nm and 630 nm for $D = 80$ nm. For the RLCA clusters (Figure 7a), the peak position increases slowly with the number of particles. However, the compact cluster spectra (Figure 7c) red-shift rapidly with increasing cluster size. The results for the 80 nm particles in Figure 8 show similar behavior. Figure 9 shows the dependence of peak wavelength on cluster size. Here, we see that, for a given number of particles in the cluster, the peak position shifts much more rapidly to long wavelength as the fractal dimension increases.
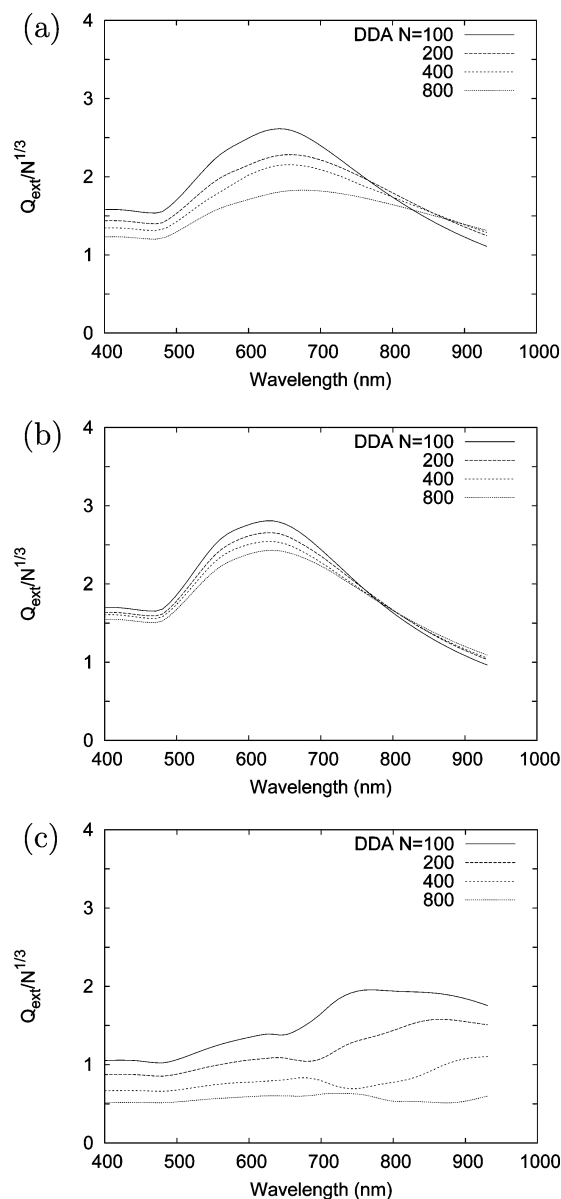
Figures 7 and 8 show that, for both the 60 and 80 nm particles, the plasmon peak wavelengths for the compact cluster are larger than in the experiment, Figure 2. In the dynamic scattering experiment, the hydrodynamic radii of the 60 nm aggregates are in the ranges 150−300 nm after 1 h and 230−410 nm after 5 h. If we assume that the aggregates are compact (which is consistent with the model used in analyzing the light scattering data), then with the measured value of the hydrodynamic radius of a single nanoparticle (39 nm), the numbers of particles inside the aggregates are 60−460 (after 1 h) and 210−1200 (after 5

Structures of DNA-Linked Nanoparticle Aggregates

J. Phys. Chem. B, Vol. 110, No. 25, 2006 **12679**
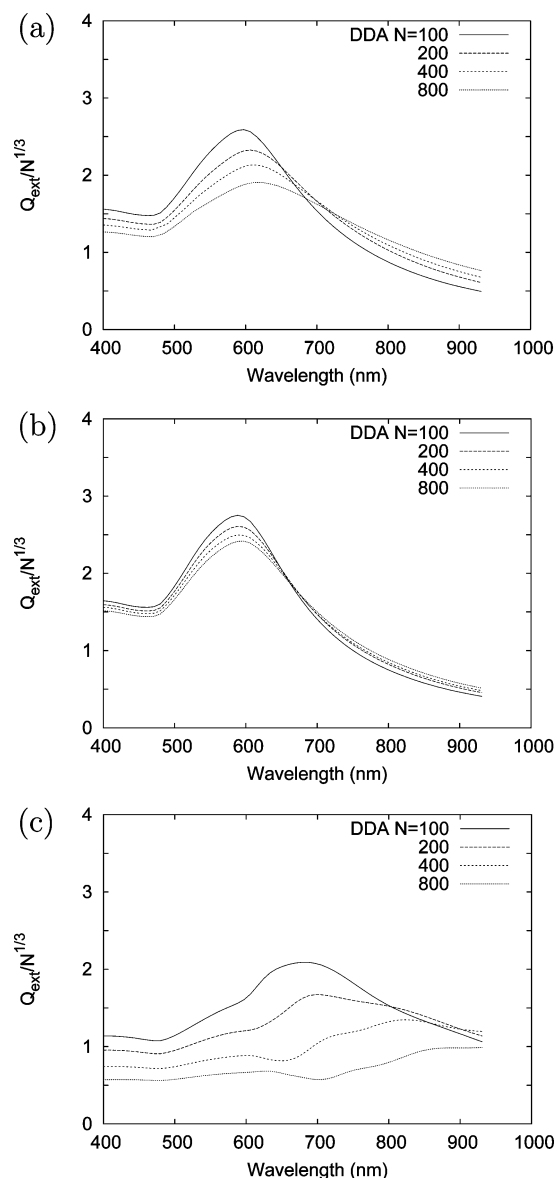
Figure 7. Calculated extinction coefficients Q_{ext} using DDA, for (a) a RLCA cluster; (b) a DLCA cluster; (c) a compact cluster in an aqueous solution, varying the number of nanoparticles N in a cluster from 100 to 800. The resulting plots were averaged over 10−100 cluster realizations. The diameter of the nanoparticles is 60 nm.

Figure 8. Calculated extinction coefficients Q_{ext} using the DDA method, for (a) a RLCA cluster; (b) a DLCA cluster; (c) a compact cluster in an aqueous solution, varying the number of nanoparticles N in a cluster from 100 to 800. The resulting plots were averaged over 10−100 cluster realizations. The diameter of nanoparticles is 80 nm.

h). Compared with the results 5 h after hybridization in Figure 2, we find that the compact cluster results in Figures 7 and 8 are far to the red of what is measured for the measured cluster size. Hence, we can conclude that the fractal structures, especially the RLCA clusters are more consistent.

Comparison of the RLCA results in Figures 7 and 8 with the results in Figure 2 show rough agreement, with the $D = 60$ nm experiments yielding peaks at 630 nm (1 h) and 670 nm (5 h) and the $D = 80$ nm experiments yielding peaks at 680 nm (1 h) and 750 nm (5 h), compared to RLCA peaks of 600 nm ($D = 60$ nm) and 650 nm ($D = 80$ nm) based on DDA calculations (for 200 particles) and 610 and 670 nm from T-matrix theory (for 100 particles). The systematic red-shift of the experiments compared to theory could have several possible explanations, including the contributions of very large aggregates, which we mentioned earlier were apparent in the light-scattering results, and local structure changes due to low rigidity of the aggregates. The inclusion of larger clusters will red-shift the plasmon peaks as is clear from Figure 9, although it would take 10 000 particle clusters to exactly fit the experimental data. Local structural

changes due to lack of rigidity could lead to a fractal dimension larger than 2.07,[28] so on the basis of Figure 9, this should lead to plasmon peaks at longer wavelengths. Whatever reason it might be, it seems reasonably clear that the fractal clusters with the fractal dimension close to the RLCA value can explain the experimental results reasonably well.

We now examine the robustness of the peak positions obtained for the different cluster models, i.e., we check whether variations in cluster structure that reflect unknown or uncontrollable factors in the experiments would change the conclusions of the previous paragraph. First, we increase the edge-to-edge distance from 12 to 16 nm, while keeping the nanoparticle diameter at $D = 60$ nm. The results are shown in Figure 10a based on T-matrix calculations. This shows that the peak positions for the three clusters shift slightly to shorter wavelengths (by about 20 nm for the fractal clusters) as the particle separation is increased. This shift does not change the distinction between the fractal clusters (RLCA or DLCA) and the compact cluster, and the size of the wavelength shift is small enough
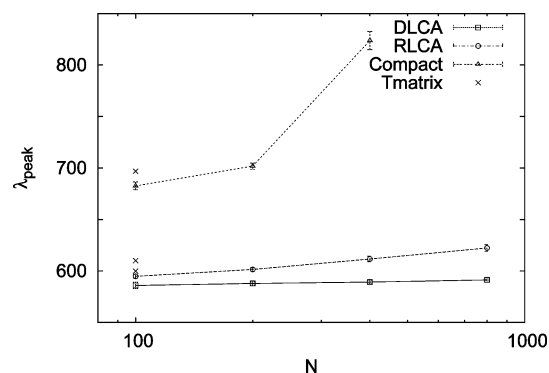
Figure 9. Size dependence of the peak position λ_{peak} of extinction coefficients using DDA, for RLCA, DLCA, and compact clusters in an aqueous solution, varying the number of nanoparticles N in a cluster from 100 to 800. The resulting plots were averaged over $10-100$ cluster realizations. The diameter of nanoparticles is 60 nm. The crosses denote the peak position of extinction coefficients using T-matrix with 100 nanoparticles, for (from the bottom), DLCA, RLCA, and compact clusters.

that it is hard to distinguish between these two particle separations in the comparison with experiment. Second, we randomly varied the diameter of the particles up to 5% from $D = 60$ nm. Here, we used the RLCA structure, and made 10 realizations of the distribution of particle diameters. Thus, the particles in the cluster lie on sites in a cubic lattice designed for an average edge-to-edge distance of 12 nm, but because of variations in particle diameter, this distance will also vary. The T-matrix results are presented in Figure 10b, and we see little change due to variation in particle diameter. Finally, we consider optical properties from off-lattice models. To do this, we have generated a fractal cluster based on the off-lattice diffusion-limited aggregation (DLA) model of ref 42, and we have generated a compact cluster using an optimized Lennard-Jones (LJ) cluster from ref 43. With the T-matrix model (the DDA model can only be used for on-lattice structures), the calculated extinction coefficients for these clusters are shown in Figure 10c. We see that the data do not change from the results of the corresponding on-lattice models, which demonstrates the insensitivity of our results to details of the structure model. Also in Figure 10c, we present the result of a spherically shaped body-centered-cubic (BCC) cluster, and it shows that the underlying crystalline lattice of clusters does not change the result significantly, although the peak position of the BCC cluster is at a slightly higher wavelength.

6. Discussion

Our results show that the measured extinction spectra associated with 60 and 80 nm gold nanoparticle aggregates generated at room temperature are consistent with fractal structures. We considered two different fractal aggregation models: diffusion-limited and reaction-limited cluster-cluster aggregation models of the aggregate structure. As the fractal dimension increases, the red-shift in the spectra tends to get bigger. The best fit to the experimental results was found for the reaction-limited cluster-cluster aggregation model.

The observed fractal structures are consistent with irreversible aggregation kinetics that is expected at room temperature when the dissociation lifetime of the DNA duplexes becomes long compared to the aggregate formation time. Our measurements of the extinction at 260 nm also suggest that there is restructuring of the aggregates toward more compact structures as temperature is increased toward the melting temperature. Although we did not characterize these higher-temperature structures directly,
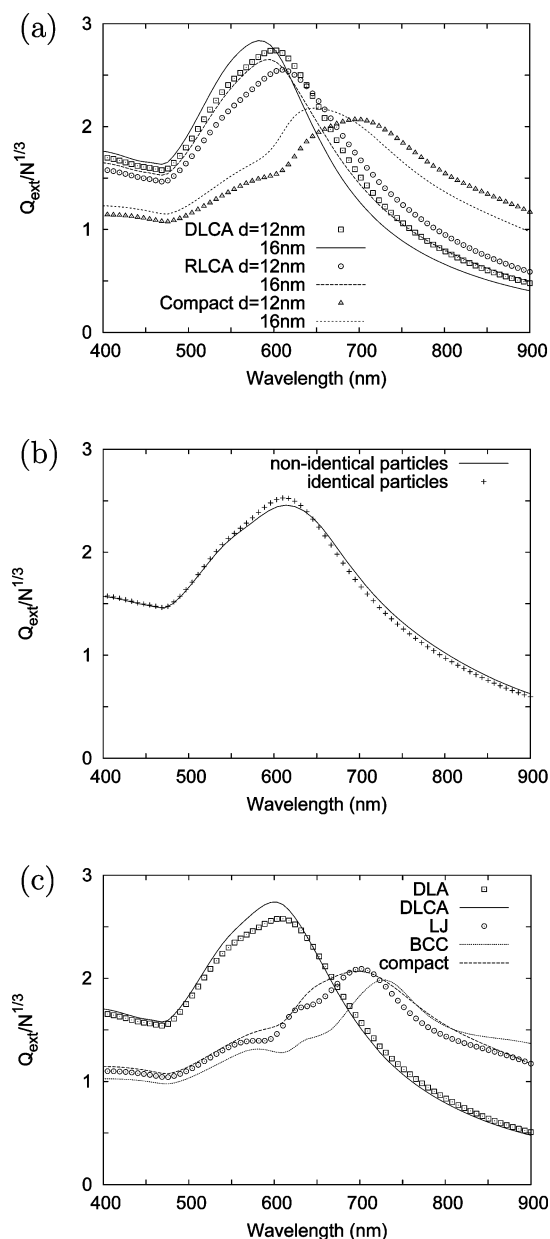
Figure 10. T-matrix spectra for the 60 nm particle aggregates in an aqueous solution, showing the effect of (a) changing the edge-to-edge distance d from 12 to 16 nm; (b) varying the particle diameters by 5%; (c) considering off-lattice models (DLA and LJ) compared to on-lattice models (DLCA, BCC, and compact). The number of nanoparticles N is 100.

there are several results that support this conclusion. First, the measured decrease in extinction at 260 nm as temperature is increased is not observed when the same aggregates are made by cooling slowly from right below the melting temperature, as presented in Figure 11a. Instead, the extinction below the melting temperature decreases as temperature decreases, which means that this method of preparation of the aggregates produces more compact structures. UV−vis spectra in Figure 11b support this interpretation. However, another possible explanation could be a sedimentation effect, but similar behavior has been observed in (much lighter) DNA−hybrid polymer aggregates[44] that do not appear to precipitate. Second, our theoretical calculations show that the extinction at short wavelength (below 520 nm) is always higher in the fractal structures than in compact structures. Indeed, the extinction at 400 nm in Figure 8c is a factor of 2 lower than in Figure 8a and b, and we find similar behavior at 260 nm (not shown). A simple explanation of this is that, at

Structures of DNA-Linked Nanoparticle Aggregates

J. Phys. Chem. B, Vol. 110, No. 25, 2006 **12681**
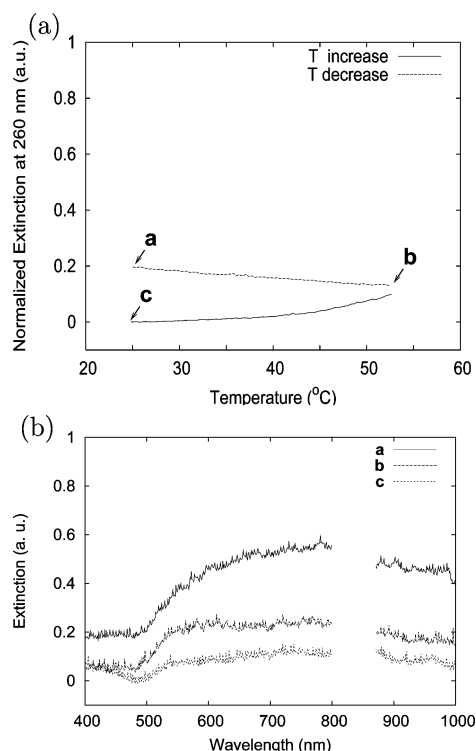
Figure 11. Temperature dependence of the extinction spectra of DNA-linked Au nanoparticle ($D = 80$ nm) aggregates. (a) Temperature dependence of the extinction at 260 nm. Extinction at 260 nm was recorded at 1 °C intervals at a rate of 1 min/deg from 25 to 52 °C (T increase) and from 52 to 25 °C (T decrease). During the temperature change, we also measure the UV–vis extinction spectra at three different points, which are denoted **a**, **b**, and **c**. (b) UV–vis spectra of DNA-linked nanoparticles with linker DNA strands with the diameter $D = 80$ nm at the points which we indicate in Figure 11a: **a** at 25 °C in the beginning of the experiment; **b** at 52 °C; **c** at 25 °C in the end of the experiment.

short wavelength, interband transitions dominate the optical response, and the clusters are optically dense.[45] This means that the spectra are dominated by absorption by the exposed surface area of the aggregate, and for a given number of particles, the less dense fractal structure will have the higher area, and hence larger extinction. Finally, SAXS measurements using annealed DNA-linked nanoparticle solutions just below the melting temperature show that for 13 nm particles the aggregates have compact structures.[16]

This restructuring behavior also has been observed simultaneously in various other unannealed DNA-linked nanocomposite aggregates that show the sharp melting,[3,4,9,10,12] and thus, this result reflects the significant contribution of large and dense aggregates to the sharp melting, although it cannot explain the exact mechanism of the sharp melting.

As a final discussion, we note that the observed red-shifts associated with aggregation are larger for the 60 and 80 nm particle aggregates than for 13 nm particle aggregates. Since the 60 and 80 nm particles produce aggregates that show sharp melting behavior, these should have superior properties for DNA sensing applications.

Supporting Information Available: Dynamic light scattering experiment. This material is available free of charge via the Internet at http://pubs.acs.org.

References and Notes

(1) Mirkin, C. A.; Letsinger, R. L.; Mucic, R. C.; Storhoff, J. J. *Nature (London)* **1996**, *382*, 607–609.
(2) Alivisatos, A. P.; Johnsson, K. P.; Peng, X.; Wilson, T. E.; Loweth, C. J.; Bruchez, Jr., M. P.; Schultz, P. G. *Nature (London)* **1996**, *382*, 609–611.
(3) Elghanian, R.; Storhoff, J. J.; Mucic, R. C.; Letsinger, R. L.; Mirkin, C. A. *Science* **1997**, *277*, 1078–1081.
(4) Storhoff, J. J.; Elghanian, R.; Mucic, R. C.; Mirkin, C. A.; Letsinger, R. L. *J. Am. Chem. Soc.* **1998**, *120*, 1959–1964.
(5) Mucic, R. C.; Storhoff, J. J.; Mirkin, C. A.; Letsinger, R. L. *J. Am. Chem. Soc.* **1998**, *120*, 12674–12675.
(6) Shchepinov, M. S.; Mir, K. U.; Elder, J. K.; Frank-Kamenetskii, M. D.; Southern, E. M. *Nucleic Acids Res.* **1999**, *27*, 3035–3041.
(7) Nelson, D. R. *Nano Lett.* **2002**, *2*, 1125–1129.
(8) Tkachenko, A. V. *Phys. Rev. Lett.* **2002**, *89*, 148303.
(9) Strable, E.; Johnson, J. E.; Finn, M. G. *Nano Lett.* **2004**, *4*, 1385–1389.
(10) Gibbs, J. M.; Park, S.-J.; Anderson, D. R.; Watson, K. J.; Mirkin, C. A.; Nguyen, S. T. *J. Am. Chem. Soc.* **2005**, *127*, 1170–1178.
(11) Biancaniello, P. L.; Kim, A. J.; Crocker, J. C. *Phys. Rev. Lett.* **2005**, *94*, 058302.
(12) Storhoff, J. J.; Lazarides, A. A.; Mucic, R. C.; Mirkin, C. A.; Letsinger, R. L.; Schatz, G. C. *J. Am. Chem. Soc.* **2000**, *122*, 4640–4650.
(13) Park, S.-J.; Lazarides, A. A.; Mirkin, C. A.; Brazis, P. W.; Kannewurf, C. R.; Letsinger, R. L. *Angew. Chem.* **2000**, *39*, 3845–3848.
(14) Lazarides, A. A.; Schatz, G. C. *J. Phys. Chem. B* **2000**, *104*, 460–467.
(15) Lazarides, A. A.; Schtaz, G. C. *J. Chem. Phys.* **2000**, *112*, 2987–2993.
(16) Park, S.-J.; Lazarides, A. A.; Storhoff, J. J.; Pesce, L.; Mirkin, C. A. *J. Phys. Chem. B* **2004**, *108*, 12375–12380.
(17) Park, S. Y.; Stroud, D. *Phys. Rev. B* **2003**, *68*, 224201.
(18) Meakin, P. *Adv. Colloid Interface Sci.* **1988**, *28*, 249–331.
(19) Jin, R.; Wu, G.; Li, Z.; Mirkin, C. A.; Schatz, G. C. *J. Am. Chem. Soc.* **2003**, *125*, 1643–1654.
(20) Kiang, C.-H. *Physica A* **2003**, *321*, 164–169.
(21) Goodrich, G. P.; Helfrich, M. R.; Overberg, J. J.; Keating, C. D. *Langmuir* **2004**, *20*, 10246–10251.
(22) Park, S. Y.; Stroud, D. *Phys. Rev. B* **2003**, *67*, 212202.
(23) Lukatsky, D. B.; Frenkel, D. *Phys. Rev. Lett.* **2004**, *92*, 068302.
(24) Lukatsky, D. B.; Frenkel, D. *J. Chem. Phys.* **2005**, *122*, 214904.
(25) Rosi, N. L.; Mirkin, C. A. *Chem. Rev.* **2005**, *105*, 1547–1562.
(26) Harris, N. C.; Kiang, C.-H. *Phys. Rev. Lett.* **2005**, *95*, 046101.
(27) Morrison, L. E.; Stols, L. M. *Biochemistry* **1993**, *32*, 3095–3104.
(28) Lin, M. Y.; Lindsay, H. M.; Weitz, D. A.; Ball, R. C.; Klein, R.; Meakin, P. *Phys. Rev. A* **1990**, *41*, 2005–2020.
(29) Stradner, A.; Sedgwick, H.; Cardinaux, F.; Poon, C. K.; Egelhaaf, S. U.; Schurtenberger, P. *Nature (London)* **2004**, *432*, 492–495.
(30) Brown, W. D.; Ball, R. C. *J. Phys. A* **1985**, *18*, L517–L521.
(31) Meakin, P. *Phys. Rev. Lett.* **1983**, *51*, 1119–1122.
(32) Kolb, M.; Botet, R.; Jullien, R. *Phys. Rev. Lett.* **1983**, *51*, 1123–1126.
(33) Purcell, E. M.; Pennypacker, C. R. *Astrophys. J.* **1973**, *186*, 705–714.
(34) Goodman, J. J.; Draine, B. T.; Flatau, P. J. *Opt. Lett.* **1991**, *16*, 1198–1200.
(35) Draine, B. T.; Flatau, P. J. *J. Opt. Soc. Am. A* **1994**, *11*, 1491–1499.
(36) Waterman, P. C. *Phys. Rev. D* **1971**, *3*, 825–839.
(37) Peterson, B.; Ström, S. *Phys. Rev. D* **1973**, *8*, 3661–3678.
(38) Mackowski, D. W. *J. Opt. Soc. Am. A* **1994**, *11*, 2851–2861.
(39) Mackowski, D. W.; Mishchenko, M. I. *J. Opt. Soc. Am. A* **1996**, *13*, 2266–2278.
(40) The molar extinction coefficients are calculated from the measured UV–vis absorbance of a colloid with a known particle concentration.
(41) Yanagi, K.; Prive, G. G.; Dickerson, R. E. *J. Mol. Biol.* **1991**, *217*, 201–214.
(42) Witten, T. A., Jr.; Sander, L. M. *Phys. Rev. Lett.* **1981**, *47*, 1400–1403.
(43) Northby, J. A. *J. Chem. Phys.* **1987**, *87*, 6166–6177.
(44) Gibbs, J. M.; Nguyen, S. T. Private communications.
(45) Park, S. Y.; Schatz, G. C. Unpublished work.